ADAPTIVE MULTIRATE DATA ACQUISITION OF 3D CELL IMAGES

T.E. Merryman[1]*, J. Kovačević* [1,2]*, E. Garcia Osuna*[2] *and R.F. Murphy*[2,3]

Carnegie Mellon University, Center for Bioimage Informatics
Departments of Electrical and Computer Engineering[1], Biomedical Engineering[2] and Biological Sciences[3]
5000 Forbes Ave., Pittsburgh, PA 15213
<tadm@cmu.edu, jelenak@cmu.edu, eog@andrew.cmu.edu, murphy@cmu.edu>

ABSTRACT

We present an algorithm for efficient acquisition of fluorescence microscopy data sets, a problem not addressed until now in the literature. We do this as part of a larger system for protein classification based on their subcellular location patterns, and thus strive to maintain the achieved level of classification accuracy as much as possible. This problem is similar to image compression but unique due to additional restrictions, namely causality; we have access only to the information that has been scanned up to that point. While we do want to acquire fewer samples with as low distortion as possible to achieve compression, our goal is to do so while affecting the overall classification accuracy as little as possible. We achieve this by using an adaptive multiresolution scanning scheme which samples the regions of the image area that hold the most pertinent information. Our results show that we can achieve significant compression which we can then use to increase either time of space resolution of our data set, all while minimally affecting the classification accuracy of the entire system.

1. INTRODUCTION

The motivation for finding an efficient way of acquiring cellular images is great. In fluorescence microscopy, the confocal scanning microscope is one of the most often used and it scans the field pixel by pixel [1]. Photo-bleaching occurs each time the laser used to excite the region being imaged focuses on a pixel. The exposure time and laser intensity both play a major part in photobleaching. By reducing the number of samples (maximum resolution locations) we need to scan, we save time which could be used to speed up the acquisition process or in tradeoffs to reduce the laser intensity (reduce the effects of photo-bleaching) and increase the resolution in other dimensions [2]. One could reduce the number of samples acquired by using traditional sampling algorithms but effects of aliasing would distort the approximation images [3]. We aim here for an adaptive, efficient algorithm that would scan fewer pixel locations, while limiting the distortion and maintaining as much information as possible about the distribution of fluorescence in the sample. This requires some means of evaluation, and for this we build on prior work demonstrating that machine classifiers can recognize all mojor subcellular patterns in 3D images of cultured cells with high accuracy [4, 5, 6]. We can thus compare the classification accuracy for adaptively sampled images to that for the original images to assess the degree of preservation of image information content.

This work was supported in part by NSF-ITR grant EF-0331657.

The previoius work in this area focused on the process of recovery rather than different approaches of data acquisition [2, 8, 9]. Trying to efficiently acquire cellular images using adaptive sampling methods is new.

We will work with 3D images (cell volumes) that have the maximum resolution in each of the three dimensions. We will run our multirate data acquisition algorithm using different input parameters on each of these data sets to simulate the acquisition from the microscope and build a synthesized data set of adaptively sampled images. We will then compare these images to the original images and examine their rate-distortion curves to find where the algorithm works optimally. We will do the same with standard downsampling using bilinear interpolation. This rate-distortion measure will give a general insight to the performance of the algorithm. Although the rate-distortion gives us valuable information, our goal is to eventually reduce the number of samples while maintaining the classification accuracy of the system. We will thus measure the compression ratio with respect to the classification accuracy.

2. MOLECULAR IMAGING

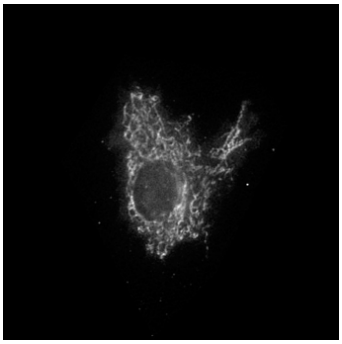

Fig. 1. Image of a mitochondrial protein pattern.

Fig. 1 points to the properties of the data sets we will be working with. Observe how the image is predominantly dark with mostly low pixel intensities. This observation leads us directly to the most important assumption: High frequencies (rapid changes in pixel intensities among neighboring pixels) will only occur in a small percentage of the area contained within the image boundaries.

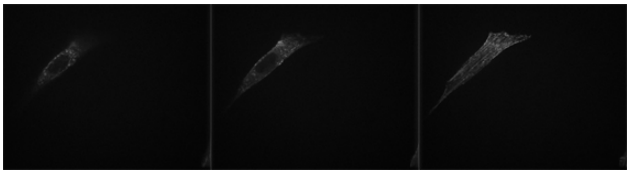

Fig. 2. Images from a 3D sequence of actin protein pattern.

Fig. 2 shows that neighboring slices share similar patterns and locations in the 3D image of actin.

With these observations in mind, we can make a strong argument for a multirate approach. When standard downsampling is used and then interpolated back to the maximum resolution using bilinear interpolation, all of the high-frequency content is not only lost but is misrepresented as a result of aliasing. In the dark regions of the images, only low frequencies are present. These low frequencies can be captured with few samples. In contrast, areas where high-intensity values are located, there are high frequencies that need to be represented using a greater number of samples. Using different sampling rates in acquiring the data set is called multirate sampling. The images of subcellular protein locations we examine in this work do not share the same location patterns and thus the distribution of frequencies across the images varies. This is the reason for an adaptive multirate approach.

3. MULTIRATE ACQUISITION OF CELLULAR IMAGES

The block diagram of our adaptive multirate algorithm is shown in Fig. 3 and repeated for each slice of the 3D image. This is the major component of the overall system that constructs an approximation to the original cellular data set. We now explain the algorithm in more detail.

A cell to be scanned is placed on a confocal scanning microscope. In the experiments we completed, we ran our algorithm on images scanned by the microscope at maximum resolution [4]. Using these images we created a model for guiding the microscope's scanning protocol to implement our adaptive multirate sampling algorithm.

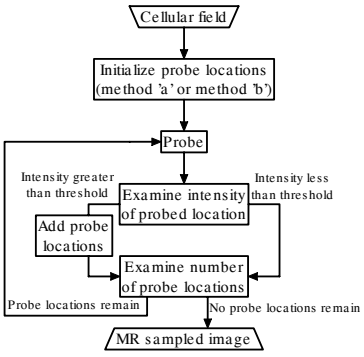

Fig. 3. Block diagram for the adaptive multirate sampling algorithm.

Probe locations are initialized in one of two ways: The first is to set up probe locations throughout the entire cellular field rectangularaly at 8 or 16 primary units apart (primary unit refers to the basic element of the maximum resolution). This can be seen in Fig. 4. The grid in the figure represents all of the possible spaces where samples can be drawn from the cellular field or in our simulation from the original maximum resolution image. Initializing the probes in this fashion begins the sampling process assuming that most of the area contained within the boundaries of the photographable region hold only low frequencies. The second way in which the probe locations are initialized uses cellular location knowledge that has already been acquired from previous slices in the 3D sequence. Fig. 2 shows that cell locations in adjacent slices are very similar. When stepping through the sampling process, it is efficient to rule out areas unlikely to contain any pertinent information. Fig. 5 shows how to initialize the probe locations if we can guess where the cell protein structure is located. We will elaborate on this in what follows.

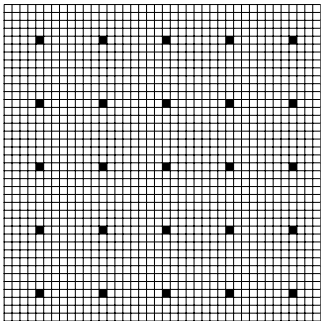

Fig. 4. This grid gives a graphic view of how the sampling or probe locations are initialized. Each block represents a possible probe location and the black blocks represent where a probe location has been initialized.

These two methods for initializing the probe locations are used in different situations: the first method when there is no information available about the location of the cell protein structure, while the second one is used when information is available. To add more robustness to the system, the first method can be used periodically even when knowledge about the location is known.

When there are locations remaining to be probed, the microscope will move to these locations and record the intensity of the light emitted from the cellular field when exposed to the laser. Probing occurs until there are no more locations left to be examined. In our simulation, a probe is represented by taking a sample from the maximum resolution original image at a specific pixel location.

After a location is probed and an intensity value is returned it is compared to a threshold. The threshold is set by the user and determines the sensitivity of the algorithm. A lower threshold will raise the sensitivity and take more samples while a higher threshold will regard more locations to be uninteresting. When a pixel's intensity is examined one of two things occurs: If the value is greater than the threshold, then the value is stored in what is called a foreground image. The foreground image is an image that contains all of the intensity values gathered from probes where the intensity exceeds the threshold. After this value is stored, new probes are added to the grid. The initial distance between probe locations is 8. New areas to scan will be added as shown in Fig. 6. Probes are added in the extended neighborhood of this pixel. The extended neigh-

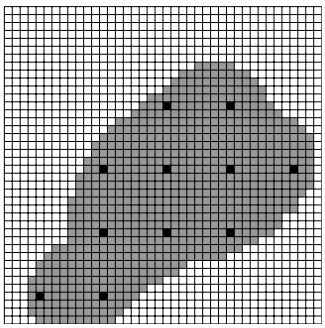

Fig. 5. This grid gives a graphic view of how the sampling or probe locations are initialized. Each block represents a possible probe location. Black blocks represent where a probe location has been initialized. The oblique blob represents the assumed area where the valuable cellular information is located. The probe locations are only set up in the area where the cell is believed to be located.

borhood is (1.5) $\times$ (units away from current unit) from the current location. In the figure, the distance between probe locations (black pixels) is 8 units. In part (a), the gray pixels represent the probe locations added when the circled probe location reveals a value that is greater than or equal to the threshold. This is a recursive process and its next step is shown in part (b) of the same figure.

If the value returned from the probe at a certain location does not exceed the threshold, then that value is also stored in what is called the background image. The background image consists of all the probed locations that are smaller than the threshold. When all of the probe locations have been examined, the background image is interpolated to the size of the original image. When all probes are completed, the approximated image is constructed. The approximated image is set equal to the background image where the foreground image is without an intensity value.

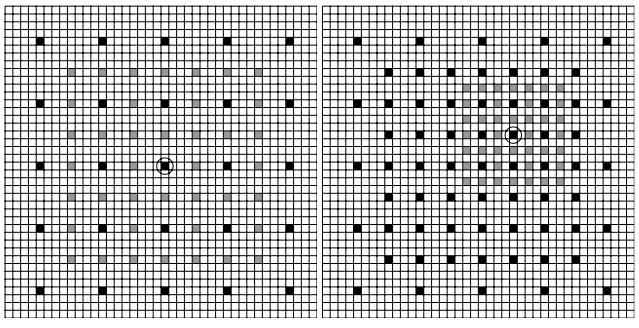

(a) (b)

Fig. 6. (a) This grid shows the process for adding probe locations (in gray). when probed value is greater than the threshold. (b) This shows the recursive nature of the same process when a new probe location exceeds the threshold and more probe locations are added at a finer resolution.

To create a more efficient algorithm and to save even more probes, we can use the information about the cell protein structure location from the previous slice that has been approximated. This is done by creating a mask. The mask examines the foreground image of the neighboring slice. We convert the foreground image into a binary image where 1 signifies where the foreground image has positive intensities and 0 signifies no intensity. This image is expanded by the morphological operation of dilation. This creates a mask that is larger than the area where the structure was located in the previous slice and compensates for any growth or movement of the cell. In the subsequent slice, we will only initialize the probe locations that lie in the region where the mask is located. For 2D cellular images, the masking step is omitted. With those images, the algorithm never assumes to have knowledge of the protein location and always intializes the probe locations using the first method of initialization described earlier in this section.

4. EXPERIMENTAL RESULTS

We synthesized the cellular field by using four sequences of images. Each of the sequences has $1024\times1280\times30$ resolution. After processing each of the sequences we compared them to the original sequences. We found the mean-squared error for different thresholds which affect the number of samples taken. We also repeated the process with standard downsampling and bilinear interpolation and compared the results. Table 1 gives the optimal compression ratio and MSE for the four 3D data sets we tested. Note that the compression ratios are close but the distortion is higher for the standard downsampled approximations. Mean squared error is given by:

$$MSE = \frac{1}{MNI}\sum_{m=0}^{M}\sum_{n=0}^{N}\sum_{i=0}^{I}(X_{mni} - Y_{mni})^2,$$

where X is the original sequence and Y is the approximated sequence whose values range from 0 to 255. M, N and I are parameters that describe the dimensions of the image.

Data	*Multirate Compression Ratio*	*Multirate MSE*	*Standard Comression Ratio*	*Standard MSE*
Actin	34:1	14	36:1	18
Mito	56:1	4	49:1	19
Nucleus 1	122:1	14	121:1	22
Nucleus 2	113:1	13	100:1	30

Table 1. Compression ratios and MSE for four 3D data sets. The results are given for the multirate algorithm and the standard algorithm.

We next evaluated classification accuracy for images acquired with the downsampling methods. We began by running the multirate and standard downsampling algorithms on a bank of 500 2D images of size 512×512 [7]. These images represent 10 distinct classes (proteins). We then calculated the features based on SLF-5 minus the DNA features for each of the approximated images and used a Support Vector Machine (SVM) to classify[10]. Fig. 7 shows that the accuracy decline with standard downsampling is more drastic than that of the multirate downsampling. Table 2(a) gives the accuracy of the original images. Table 2(b) shows the same detailed accuracy for multirate downsampling with a compression ratio of 9:1. Table 2(c) shows the accuracy result with a compression ratio of 4:1. Note that the overall accuracy is identical for parts (b) and (c); however, the standard downsampling achieves

this measure with more than twice the number of samples used by the multirate approach.

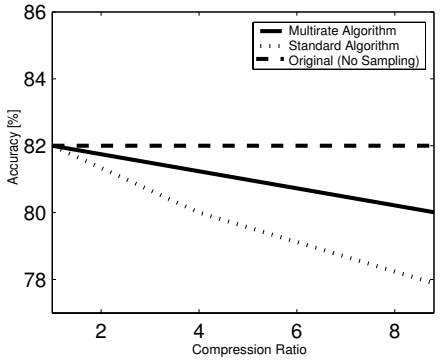

Fig. 7. Classification accuracy of the original system (no sampling), multirate algorithm, and standard algorithm.

5. CONCLUSIONS

We presented a scheme for adaptive multirate acquisition of 3D cell images. We found that the intelligent acquisition of multirate downsampling outperforms standard downsampling. In a rate-distortion sense, it out performs because it retains the high frequencies and saves samples where low frequencies are present. In a classification accuracy sense, the multirate algorithm also outperforms standard downsampling as it retains a better classification accuracy for higher compression rates than standard downsampling.

6. ACKNOWLDGEMENTS

We would like to thank Prof. Tsuhan Chen for valuable comments. We would also like to thank Ting Zhao for the use of his feature calculation code and SVM classifier code.

Original Image Accuracy (no sampling)

	Output of Classifier									
Input	DNA	ER	Gia	Gpp	L2	Mit	Nuc	Act	TfR	Tub
DNA	94	2	0	0	0	0	0	0	4	0
ER	2	82	0	0	2	2	0	0	0	12
Gia	0	0	84	10	0	0	4	0	2	0
Gpp	0	0	8	80	6	0	2	0	2	2
L2	0	0	0	2	80	0	0	0	16	2
Nuc	0	2	0	0	0	82	0	0	6	10
Mit	2	0	0	0	4	0	92	0	2	0
Act	0	0	0	0	0	0	0	100	0	0
Tfr	2	2	0	0	18	8	0	2	56	12
Tub	0	8	0	0	2	8	0	0	12	70

(a)

Average accuracy: 82%

Accuracy with Multirate Algorithm

	Output of Classifier									
Input	DNA	ER	Gia	Gpp	L2	Mit	Nuc	Act	TfR	Tub
DNA	82	2	0	0	2	0	2	0	12	0
ER	4	76	0	0	6	0	0	0	2	12
Gia	0	0	84	4	6	0	4	0	2	0
Gpp	0	0	8	76	10	0	2	0	2	2
L2	0	2	0	2	86	0	0	0	10	2
Nuc	0	4	0	0	2	78	0	0	6	10
Mit	4	0	2	0	4	0	88	0	2	0
Act	0	0	0	0	0	0	0	100	0	0
Tfr	2	2	0	2	18	4	0	2	54	16
Tub	0	8	0	2	4	4	0	0	6	76

(b)

Average accuracy: 80%, Compression Ratio: 9.8:1

Accuracy with Standard Algorithm

	Output of Classifier									
Input	DNA	ER	Gia	Gpp	L2	Mit	Nuc	Act	TfR	Tub
DNA	92	2	0	0	0	0	0	0	4	2
ER	2	88	0	0	0	0	0	0	0	10
Gia	0	0	82	12	0	0	4	0	2	0
Gpp	0	0	8	82	6	0	0	0	2	2
L2	0	4	0	2	78	0	0	0	16	0
Nuc	0	6	0	0	2	74	0	0	10	8
Mit	4	0	2	0	2	0	90	0	2	0
Act	0	0	0	0	0	0	0	98	2	0
Tfr	2	2	0	0	16	8	0	6	52	14
Tub	0	8	0	0	2	12	0	0	14	64

(c)

Average accuracy: 80%, Compression Ratio: 4:1

Table 2. Detailed classification accuracy for (a) no sampling, (b) multirate sampling algorithm and (c) standard downsampling algorithm.

7. REFERENCES

[1] C. J. Cogswell, K. Carlsson (1994). "Three-dimensional microscopy: image acquisition and processing." *SPIE.* Bellingham, Washington, USA.

[2] J. C. Bulinski, D. J. Odde, Bo. J. Howell, T. D. Salmon and C. M. Waterman-Storer (2001). "Photobleaching and recovery of ensconsin chimera in untreated cells. Rapid dynamics of the microtubule binding of ensconsin in vivo." *Journal of Cell Science.* 114:3885-3897.

[3] M. Kostic (1999). "The art of signal sampling and aliasing: simulation with a LabVIEW virtual instrument – what we see is not what it is!" *NIWeek 99 Annual Conference*, National Instruments, Austin, TX, 1999. www.kostic.niu.edu/NIWEEK99.htm

[4] M. Velliste, R.F. Murphy (2002). "Automated determination of protein subcellular locations from 3D fluorescence microscope images." " *Proc 2002 IEEE Intl Symp Biomed Imaging (ISBI 2002),* pp. 867-870.

[5] K. Huang, R. F. Murphy (2004). "Automated classification of subcellular patterns in multicell images without segmentation into single cells." *Proc 2004 IEEE Intl Symp Biomed Imaging (ISBI 2004),* pp. 1139-1142.

[6] X. Chen, R. F. Murphy (2004). "Robust classification of subcellular location patterns in high resolution 3D fluorescence microscope images." *Proceedings of the 26th Annual International Conference of the IEEE Engineering in Medicine and Biology Society,* pp. 1632-1635.

[7] M. V. Boland, R. F. Murphy (2001). "A neural network classifier capable of recognizing the patterns of all major subcellular structures in fluorescence microscope images of HeLa cells." *Bioinformatics 17:* pp. 1213-1223.

[8] K. Gonda, J. Fowler, N. Katoku-Kikyo, J. Haroldson J, Wudel J, Kikyo N.(2003). "Reversible disassembly of somatic nucleoli by the germ cell proteins FRGY2a and FRGY2b." *Nature Cell Biology* 5, 205-210.

[9] E.A.J. Reits, J.J. Neefjes (2001). "From fixed to FRAP: measuring protein mobility and activity in living cells." *Nature Cell Biology 3*, E145-147.

[10] K. Huang, M. Velliste, R. F. Murphy (2003). "Feature reduction for improved recognition of subcellular location patterns in fluorescence microscope images." *Proc. SPIE 4962*, 307-318.